

<https://doi.org/10.1038/s41524-024-01327-1>

What drives the heterogeneous interdiffusion in the Li-Si interfacial region of Si anodes: the Li flux or the Si flux?

Check for updates

Fangjia Fu^{1,2}, Xiaoxu Wang³, Taiping Hu^{2,4}, Guobing Zhou^{4,5}, Fu-Zhi Dai²✉ & Shenzhen Xu^{2,4}✉

The electrochemical reaction in silicon (Si) electrode, accompanying with tremendous volume expansion, causes rapid capacity fade of Li-ion batteries. The Li-ion concentration gradient and structural distribution uniformity influence the inhomogeneous expansion, and the kinetic mechanism of lithiation and interfacial morphology evolution remains debated. The present study focuses on the dynamics of Li-Si interdiffusion at Si/Li interfaces with various Si-facet orientations and phases using a machine-learning potential. We find that the Si flux from bulk Si to Li-Si interface regions controls the length of Li-Si interdiffusion region. The lithiation length in different Si/Li interface systems exhibits the order of amorphous-Si > crystalline-Si(110) > crystalline-Si(100) > crystalline-Si(111), which agrees with the experimental trend. Our atomic simulations further reveal that the key factor determining the Li-Si interdiffusion is the difference of on-site Si atomic energies between the bulk Si and the Li-Si interface regions. We propose that the large interdiffusion extent is due to a low thermodynamics barrier. Our findings provide insights for the development of high-performance Si anode materials.

Achieving the next generation lithium-ion (Li-ion) batteries with high energy and power densities is a critical scientific and technological challenge in the field of electrochemical energy storage^{1,2}. Especially the silicon (Si) anode, which possesses a high capacity (3579 mAh g⁻¹), is regarded as one of the most promising anode materials for enhancing the specific energy density of batteries³⁻⁶. However, the continuous phase transformations and volume expansion/contraction (up to ~300%) during the Si (de)lithiation process can significantly generate morphological defects, local Li distribution inhomogeneity and low diffusivity, which limit the improvement of rate performance and cyclic stability in Li-ion batteries^{3,7,8}. Experimental work pointed out that both crystalline and amorphous Si (c/aSi) phases undergo a two-phase process with a phase boundary between Si and a-Li_xSi phases at the initial stage of lithiation⁹⁻¹³. The volume expansion of cSi phase exhibits high anisotropy, with the fastest elongation occurring along the [110] direction and the lowest along the [111] direction^{10,14-16}. The kinetic mechanism during lithiation can be attributed to the orientation-dependent mobility of the interface through layer-by-layer peeling of the (111) Si facets generating a-Li_xSi phase, as reported by Liu et al. using in situ transmission electron microscopy (TEM)¹⁰. By contrast, the volume expansion of aSi phase exhibits isotropy. A more homogeneous structural change during aSi lithiation thus could occur with lower stress than the cSi case.

The study on the kinetic mechanism during lithiation process could help elucidate the relationship between electrode structures and the materials' performance, which can be applied to design electrode materials. By adjusting structural characteristics, it is possible to improve Li diffusion and electronic conductivity. Reducing structural distribution inhomogeneity can restrain internal stress. A typical application of this knowledge is the design of micro-nano structures of Si electrodes^{4,5,14-19}, including nanospheres, nanowires, nanoribbons and so on. For example, Cui et al. designed a small-sized nanostructured Si with rapid Li ion and electron transfer, shortening lithiation time and improving cycling performance^{14,15,17}. According to the rapid expansion of Li ions along the [110] direction, Chen et al. designed and synthesized a new-type Si nanoribbons with {110} facets, exhibiting high ionic conductivity, high stability of solid electrolyte interphase and long cyclic stability¹⁹. Those studies indicate that Si structures have an impact on various performance aspects of Si anodes, such as volume expansion, stresses, and fracture^{4,14-16,19}. Furthermore, we consider that the Li-Si interdiffusion and the anisotropic volume expansion of cSi during the first cycle may significantly influence the subsequent cyclic stability and performance, particularly in nanosized Si anodes^{5,14-16}. This implies that understanding the characteristics and dynamic diffusion of Li in aSi and cSi structures can in turn be used to design Si anode structures with improved energy density and cyclic stability. Despite various reports, the kinetic

¹School of Mathematical Sciences, Peking University, Beijing 100871, China. ²AI for Science Institute, Beijing 100084, China. ³DP Technology, Beijing 100080, China. ⁴School of Materials Science and Engineering, Peking University, Beijing 100871, China. ⁵Institute of Advanced Materials, Jiangxi Normal University, Nanchang 330022, China. ✉e-mail: daifz@aisi.ac.cn; xushenzhen@pku.edu.cn

mechanism of lithiation is extremely complicated, in which Li concentration gradient, interfacial reaction rates, and structural uniformity may combine together to play important roles. It is crucial to investigate the dynamic mechanisms and microstructural evolution at Li-Si interfaces during lithiation process at an atomic level to understand their performance.

Theoretically, reactive force field molecular dynamics (ReaxFF MD), ab initio MD (AIMD) or the climbing image-nudged elastic band (CI-NEB) transition-state (TS)-search calculations are usually performed to characterize diffusion kinetics and provide structural evolution insights into the dynamics process^{19–25}. For instance, earlier theoretical work¹⁹ reported that Li-atom migration barriers along the (100), (110), and (111) planes of bulk Si are 1.50, 1.16, and 1.88 eV, respectively, matching with the anisotropy observed in experimental measurements^{14,15}. However, this simulation study did not capture the real-time dynamic migration of Li/Si atoms and interfacial morphology evolution due to the limitation of TS-search calculations. Jin et al. reported that using the ReaxFF MD method, lithiation dynamics can be categorized into two stages: an initial mixing stage accompanied by a transition from a crystalline to an amorphous phase, and subsequently, a random walk diffusion stage²⁵. However, the accuracy of classical force field simulations is less reliable due to lack of accurate interatomic interaction descriptions in ReaxFF classical MD. Therefore, it is still a challenge to have a comprehensive and profound understanding of Li-Si interdiffusion and its dynamic mechanism, including the mobilities of Li and Si atoms and morphological changes of Li-Si interfaces in various Si phases at an atomic-scale level.

Machine learning methods have been widely applied to investigate the thermodynamic and kinetic processes of battery materials^{26–34}, including kinetic migrations, diffusion coefficients, and stabilities of crystalline and amorphous structures. Here, we employ deep potential molecular dynamic (DeePMD) simulations^{35,36} to observe dynamics of Li-Si interdiffusion in different Li/Si interface models with aSi and cSi phases, and for the cSi case, we study (100), (110) and (111) facets exposed to the Li side. The trend of lithiation length variation of the four interface models investigated in this work is consistent with the experimental observations, exhibiting the order of lithiation lengths as: aSi/Li > cSi(110)/Li > cSi(100)/Li > cSi(111)/Li. Our results reveal that the Si flux, rather than the Li flux, makes a major contribution to the evolution of the Li-Si interdiffusion extent, and the thermodynamic barrier of the on-site Si atomic energy difference between the bulk Si and the boundary of Si/Li-Si interface determines the magnitude of Si flux from bulk Si to the a-Li_xSi region, thus resulting in different lithiation extents in the four Si/Li interface models with different Si phases and surface orientations.

Results

Model construction and validation

We construct four interface models as shown in Fig. 1a–d, namely aSi/Li, cSi(100)/Li, cSi(110)/Li, and cSi(111)/Li, to reveal the kinetic mechanism of Li-Si interdiffusion and interfacial morphology evolution. The DeePMD method is employed to simulate each 5 ns trajectory starting from the initial structures of the four models. The final structure snapshots of the four

Fig. 1 | Schematic diagrams of Si/Li interface models. a–d The aSi/Li, cSi(100)/Li, cSi(110)/Li, and cSi(111)/Li interface models at the initial state ($t = 0$ ns) and the final state ($t = 5$ ns). The four snapshots on the left represent the top view (vertical to the interface) of the Si-Li interface models. The upper and bottom snapshots on the right in (a–d) represent the initial and the interdiffusion structures of our MD trajectories. The interdiffusion structures are obtained by DeePMD simulations at 500 K. The yellow and blue balls represent Si and Li atoms, respectively. **e** A schematic diagram illustrating the definitions of different regions in the Si/Li interface model after interdiffusion.

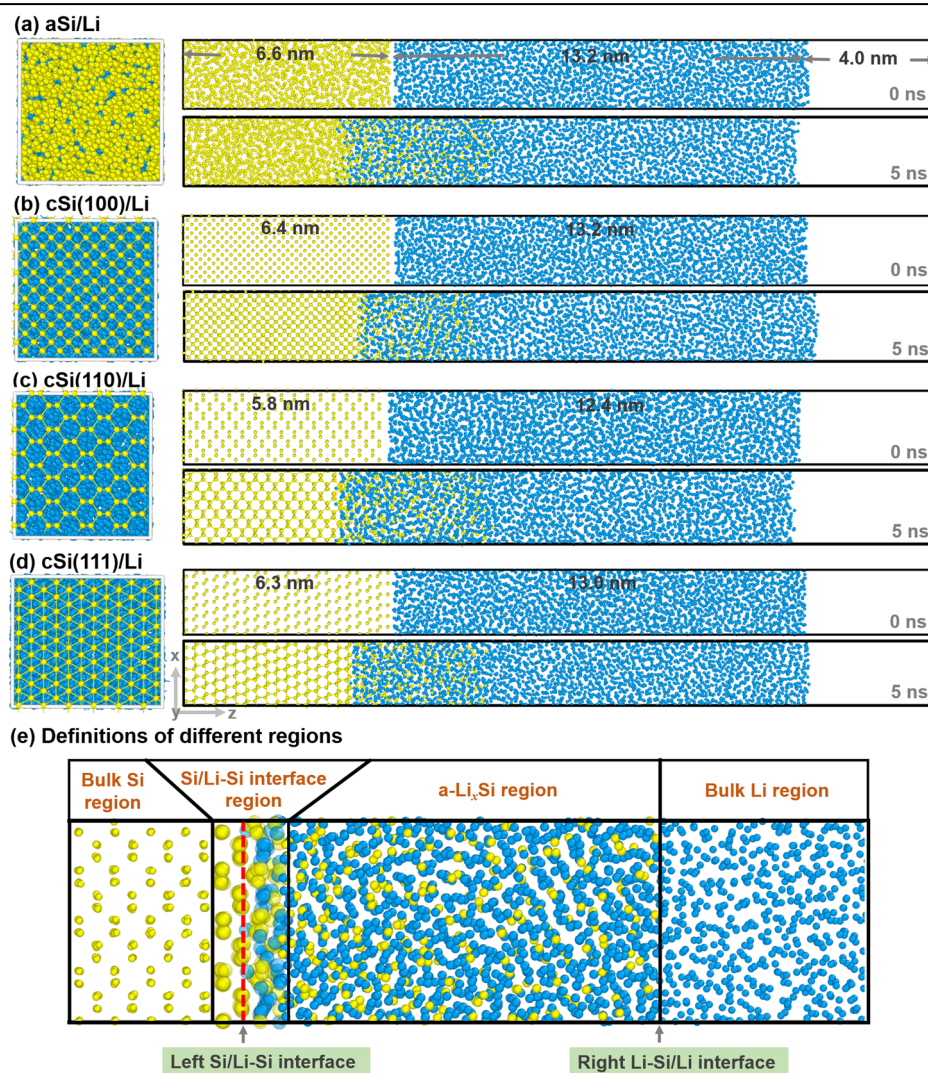
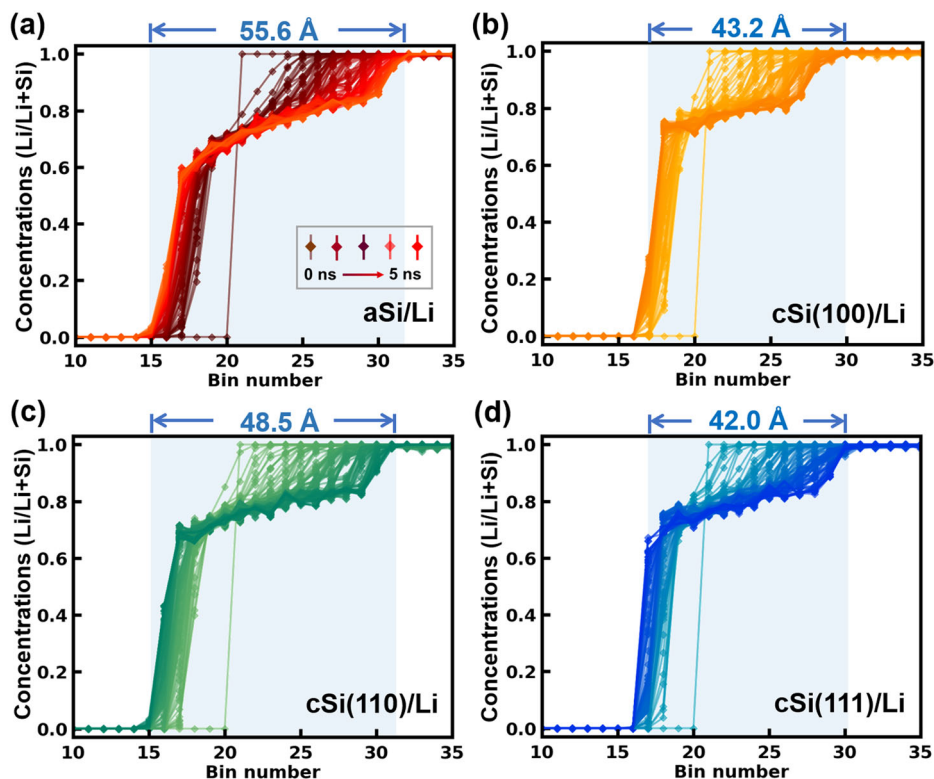


Fig. 2 | Time evolution of average Li concentration profiles. **a–d** The average Li concentration profiles along the z axis for the aSi/Li, cSi(100)/Li, cSi(110)/Li, and cSi(111)/Li interface models. Each line presents the average concentration results calculated from 50 configurations, which are sampled at equal time intervals within a period of 50 ps. 100 lines in total are included for the cSi(110)/Li model during the 5 ns DeepPMD trajectories. Fractional concentration (Li/Li+Si) means the ratio of the number of Li atoms to the total number of Li and Si atoms in each Li-Si interface model. The color representations for the time evolutions of Li fractional concentrations from 0 to 5 ns is illustrated in the inset figure of panel (a), and this pattern applies to (b–d) as well. The light blue regions and the corresponding distance values on the top in (a–d) show the lengths of Li-Si interdiffusion regions after 5 ns simulations. Note: the spatial position of simulation cells along the z axis is represented by bin numbers.



models after 5 ns simulations are also displayed in Fig. 1a–d. The supercell parameters of the four Si/Li models are listed in Supplementary Table 1. The high-accuracy DP model, which experienced a long training setup based on a specific dataset of Li-Si systems covering the entire compositional space in earlier work⁴⁹, is performed to simulate the Li-Si interdiffusion processes. The detailed setups of DP training and validation, DFT calculations and DeepPMD simulation information are presented in the methods section below.

We validate the accuracy of the Si/Li model using an independent test, which consists of a bulk aLi phase, bulk cSi and aSi phases, cSi/Li and aSi/Li interface systems with 500 configurations. It can be observed from Supplementary Fig. 1 in the Supplementary Information (SI) that the root mean square errors (RMSEs) of energy and force are 1.71 meV/atom and 0.016 eV/Å, 5.75 meV/atom and 0.128 eV/Å, 7.38 meV/atom and 0.155 eV/Å for the bulk aLi phase, bulk cSi and aSi phases, cSi/Li and aSi/Li interface systems, respectively. The RMSEs of our results are smaller than or comparable to those of previous works employing machine learning potentials for Si/Li systems^{28,37–39}. Thus, these test results indicate that our DP model exhibits a satisfactory performance for modeling the Si/Li system. As illustrated in Supplementary Fig. 2, the maximum force deviations³⁶ of cSi/Li and aSi/Li models are lower than 0.40 and 0.54 eV/Å respectively, which are similar to the test results of earlier work for battery materials⁴⁰. Compared to the crystalline models, the amorphous model shows a slightly higher deviation due to the larger configurational space. It should be noted that the tail distribution at a value of 0.54 eV/Å represents the largest deviation at a specific dimension (i.e., the force of an atom along a certain direction) among the distribution of maximum force deviations. This value is only related to one degree of freedom for a single atom in a specific structure and cannot be directly used to infer the quality of our DP model. The simulation temperature is set to 500 K to accelerate the Li-Si interdiffusion. Since the melting point of the crystalline Si phase is much higher than 500 K, this temperature setup would not significantly affect the Si crystal structures.

Furthermore, we employed the amorphous Li phase to create the Li-Si interface system based on the following reasons: (1) The solvated Li atoms in electrolytes exhibit a disordered distribution, qualitatively similar to that of

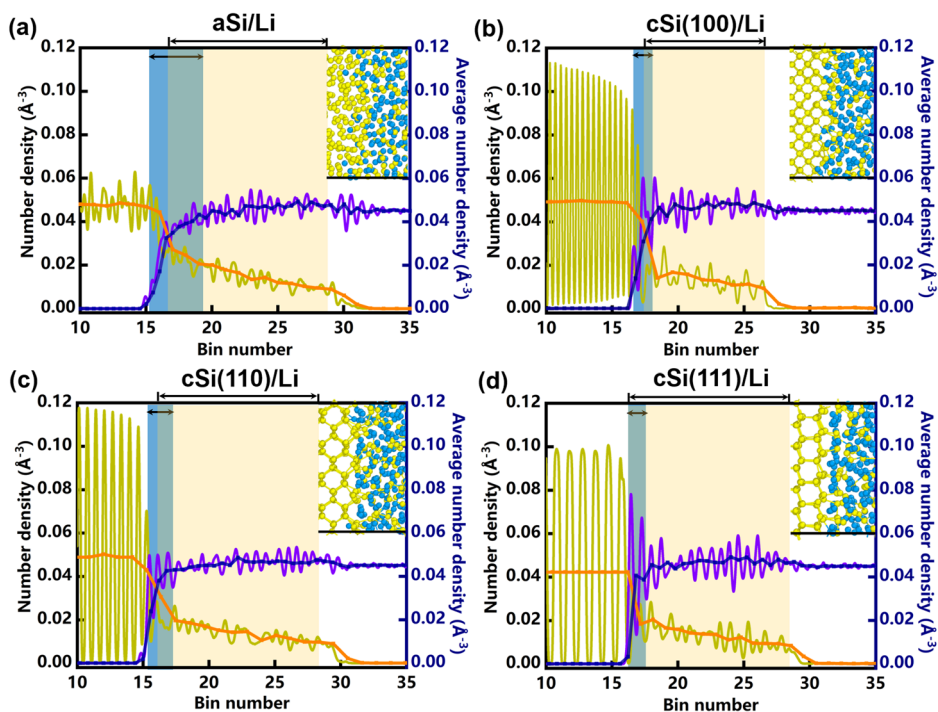
the amorphous Li phase. (2) Although we realize that the amorphous Li concentration is higher than that of the solvated Li in electrolytes in experiments, our following results in this work suggest that when Li atoms contact with the Si surface layer, the Li atoms would accumulate at the interface forming a nanoscale high-Li-concentration layer. This result is also consistent with earlier experimental observations^{16,17,41–43}, which reported that the Li migration rate along the surface of Si nanowires is significantly higher than that in the bulk, resulting in a preferential Li diffusion along the surface at first and thus leading to a high Li concentration accumulated at the surface layer. An amorphous Li slab thus could be used in the Li-Si interface model to study the dynamic lithiation process between Li atoms and Si anodes.

Lithiation length determined by Si flux

As displayed in Fig. 1e, the lithiated configuration of each Si/Li system can be defined by four different regions: the bulk Si, Si/Li-Si interface, a-Li_xSi and bulk Li regions. There are two heterogeneous interfaces in the model: one is the Si/Li-Si interface (red dashed line) on the left side, and the other is the Li-Si/Li interface (black line) on the right side. The Si/Li-Si interface region consists of a single Si layer nearest to the left of the Si/Li-Si interface and a thin layer (~3 Å) of a-Li_xSi phase nearest to the right of Si/Li-Si interface. The width of the Si/Li-Si interface region in each interface model is listed in Supplementary Table 2. We note that a single Si layer in the Si/Li-Si interface region may exhibit different widths (~2 Å–3 Å) and z -positions in the four model systems due to different layer distances between two Si layers along different facet directions.

To investigate lithiation dynamics at the Li-Si interface, time evolution of average Li concentration (Li/Li+Si) profile along the z axis are displayed in Fig. 2. We can see that the four regions exhibit different Li concentration distributions (n_{Li}): the bulk Si region has $n_{Li} = 0$, the Si/Li-Si interface and the a-Li_xSi regions correspond to $0 < n_{Li} < 1$, and the bulk Li region shows $n_{Li} = 1$. The lithiation length of the Li-Si interdiffusion region can be defined as the range from the left Si/Li-Si interface to the right Li-Si/Li interface, which covers both the Si/Li-Si interface region and the a-Li_xSi region.

Fig. 3 | Number density distributions of Si and Li atoms. a–d The number density (yellow and purple lines) and average number density (orange and dark-blue dotted lines) distributions along the z axis for the aSi/Li, cSi(100)/Li, cSi(110)/Li, and cSi(111)/Li interface models. Each line analyzes the final 200 configurations of the 5 ns DeePMD simulations. Li-Si interface morphologies of the four models are also shown in the inset figures. The light blue/orange shaded areas (whose ranges are indicated by the black arrows at top of each figure panel) show regions where the average number density of Li/Si atoms changes from 10 to 90%. Note: the spatial position of simulation cells along the z axis is represented by the bin number, and we only show part of the atomic structures of Li/Si and Li-Si interdiffusion regions in this figure for simplicity.



As shown in Fig. 2, lithiation lengths of the Li-Si interdiffusion regions in the four interface models are 55.6 Å, 43.2 Å, 48.5 Å and 42.0 Å, the corresponding trend of the Li-Si interdiffusion extent is aSi > cSi(110) > cSi(100) > cSi(111), which agrees well with the experimental results^{5,10,11}. According to the initial Li-Si boundary positions (corresponding to the dotted line at $t = 0$ ns) in Fig. 2, we find that the moving distances of the Si/Li-Si interfaces toward the left side are 19.6 Å, 13.3 Å, 18.2 Å and 12.9 Å, and the moving distances of the Li-Si/Li interface toward the right side are 36.0 Å, 29.9 Å, 30.3 Å and 29.1 Å for the aSi/Li, cSi(100)/Li, cSi(110)/Li and cSi(111)/Li models respectively. The moving speeds of the Si/Li-Si and Li/Li-Si interfaces are meaningful quantities that reflect the dynamic nature of Li-Si interdiffusion. We then calculate the average moving speeds of the Si/Li-Si and Li/Li-Si interfaces during 5 ns trajectories for the four interface models. The speeds of the left-side Si/Li-Si interfaces are 39.2 cm * s⁻¹, 26.6 cm * s⁻¹, 36.4 cm * s⁻¹, and 25.8 cm * s⁻¹, and the right-side Li/Li-Si interfaces are 72.0 cm * s⁻¹, 59.8 cm * s⁻¹, 60.6 cm * s⁻¹, and 58.2 cm * s⁻¹, respectively. This trend also exhibits the order of aSi > cSi(110) > cSi(100) > cSi(111), which is consistent to the variation of lithiation length among four models. We can see that the movement and average moving speed of the Si/Li-Si interface (the frontier of the Li diffusion) are significantly smaller than that of the Li-Si/Li interface (the frontier of the Si diffusion), indicating that the Si diffusion probably makes a more important contribution to the Li-Si interdiffusion (discussed in details with more evidence in the following sections).

Moreover, our simulation results reveal that all of the four Li-Si interface models have abrupt Li concentration (n_{Li}) gradient transition points near the boundary of the Si/Li-Si interface in the Li-Si interdiffusion regions (Fig. 2). This n_{Li} gradient transition point corresponds to the a-Li_{1.3}Si phase in the aSi/Li model and to the a-Li_{2.8}Si phase in the three cSi/Li models, respectively, which is consistent with experimental and computational results^{9,12,29}, indicating a two-phase coexistence. Our simulation results therefore are in good agreement with the trend of lithiation lengths and the phase coexistence in experimental observations^{10,13}, justifying the validity of our theoretical models.

Then, we analyze the local number density and average number density trends of Li and Si atoms in the four interface models along the z axis for the final 200 configurations in Fig. 3. As shown in Figs. 2 and 3, there are

significant differences of Li-Si interdiffusion lengths between the aSi case and the cSi cases. Moreover, among the three cSi models, the interface with the Si (110) facet exposed to Li exhibits a much longer Li-Si interdiffusion length. What are the fundamental reasons for the above phenomena? We are trying to resolve this question in the following paragraphs.

We list possible reasons which may explain the differences of lithiation lengths among the four models: (1) Since the lithiation lengths are different, one natural thought is that the structures and properties of the Li-Si interdiffusion regions may be different between the four cases, resulting in different diffusion rates of Li or Si atoms. (2) Another possibility is that, the Li-Si interdiffusion regions share similar structures and properties among the four cases, however, different magnitudes of Li flux or Si flux toward the counter side could lead to different growth speeds of the lithiation regions. If the Li flux dominates the Li-Si interdiffusion, then the distinct lithiation extents may originate from the different Li diffusion properties along different directions of Si exposed facets. (3) Analogous to the above point (2), if the Si flux dominates the Li-Si interdiffusion, then different magnitudes of Si flux toward the Li side in the four models could cause the distinct lithiation extents observed in our simulations. The definition of Li or Si flux is introduced in the methods section below. For example, the Si flux represents the average number of Si atoms moving from the bulk Si phase toward the Li phase through the Si/Li-Si interface.

We will check the validity of the above three possible explanations and exclude the unlikely ones based on data analysis of our MD simulations:

(1) For point 1, we can observe in Supplementary Fig. 3 that the trends of Li-Si coordination numbers (CN_{Li-Si}) in the a-Li_xSi regions (corresponding to the range from #18 bin to #32 bin along the x -axis) are consistent among the four models, descending from 3.75 to 0. Supplementary Fig. 4 suggests that the DP-partitioned atomic energies of Li and Si atoms within the a-Li_xSi region are almost identical among the four models. It should be noted that the DP-partitioned atomic energies of Li and Si atoms are obtained directly from the DP model, which partitions the total energy to each atom for a specific configuration (refer to SI for details). Furthermore, Fig. 3 shows that the values and trends of the average number densities of Li and Si atoms are almost identical in the a-Li_xSi regions among the four models. These observations suggest that the structures and properties within

- the a-Li_xSi regions are similar among the four models. Thus, this point can be excluded as an explanation of different Li-Si interdiffusion lengths.
- (2) Whether the Li flux dominates the Li-Si interdiffusion in the four interface models can be analyzed by comparing the three cSi/Li models, and comparing cSi/Li and aSi/Li models. On the one hand, the Li number density distributions exhibit a sharp transition at the left-side Si/Li-Si interface position as displayed in Fig. 3b–d, suggesting the Li diffusion toward the Si region is stuck in the three cSi/Li models. The Li atoms distributions along *x*-axis and *z*-axis directions in Supplementary Fig. 4 clearly show the Li atoms' accumulation at the left Si/Li-Si interface with high concentration. This Li aggregation at the cSi(111) interface emerged in our simulations is similar to the experimental characterization¹⁰, which reported the Li/Si interface shifting through layer-by-layer peeling of the (111) Si facet. On the other hand, the qualitative behavior of a relatively abrupt Li concentration transition at the left Si/Li-Si boundary still exists in the results of Fig. 3a (comparing lengths of the light-blue and the orange regions), but we can see that the Li atoms can penetrate into the aSi region to some extent in contrast to the cSi cases where the Li atoms are stuck right at the Si/Li-Si interface. All four models exhibit a similar qualitative behavior — Li flux is stuck at the Si/Li-Si boundary, however, the extents of Li diffusion into the Si side are different between the aSi vs. cSi models.
 - (3) Excluding the above (1) and (2) points, the Si flux could be the key factor driving the Li-Si interdiffusion (the last option). This also can be indicated from two observations in our simulations: The moving length of the right Li-Si/Li interface (the frontier of the Si diffusion) is notable larger than that of the left Si/Li-Si interface (the frontier of the Li diffusion), as illustrated in Fig. 2. The average number density of Si atoms changes more gradually (orange shaded areas) compared to that of Li atoms in Fig. 3, particularly for the aSi/Li and cSi(110)/Li models, indicating that the characteristic of Si diffusion is more obvious than Li. The above evidences reveal that the Si flux is likely to dominate the Li-Si interdiffusion, while the Li diffusion toward the Si region is hindered at the Si/Li-Si interface.

Then we need to provide quantitative results to differentiate the Si flux in the four models and check if the Si-flux magnitudes match with the lithiation extents in the different cases. Accordingly, our calculations show that the Si fluxes from the bulk Si phase toward the Li phase through the Si/Li-Si interface are 18.1 nm⁻² * ns⁻¹, 12.0 nm⁻² * ns⁻¹, 14.0 nm⁻² * ns⁻¹, and 10.9 nm⁻² * ns⁻¹ for the four models respectively, which are obtained from the statistical average of the complete 5 ns trajectories. This trend matches the order of the Li-Si interdiffusion lengths variation, aSi > cSi(110) > cSi(100) > cSi(111). Furthermore, the Si diffusion toward the Li side would decrease the number of Si atoms in the Si bulk region, thus causing the Si/Li-Si interface's position shifting to the left as a whole. It should be noted that the Si flux is not exactly constant throughout the whole DeepMD simulation as the quantitative flux magnitude may depend on the evolving state of the interdiffusion process and an exact steady state may not be achieved in our MD simulations considering the size limitation of our interface supercell. We thus think it is more statistically meaningful to use the time average value of Si flux rather than its specific time evolution. In addition, we find in Fig. 3 that the Li number density at the Si/Li-Si boundary exhibits an abrupt decrease to zero, the Li movement thus can be considered as a collective "shift" toward the Si phase. Due to the absence of Li concentrations on the left side of the Si/Li-Si interface, it is difficult to define a quantitative estimation of a Li flux from the bulk Li phase to the Si phase through the Si/Li-Si interface. We therefore think it is not straightforward to give an accurate and meaningful definition of the Li flux.

Mechanistic understanding on Li-Si interdiffusion

The mechanism causing the different Si flux magnitudes in the four models may be analyzed and explained from the perspective of thermodynamics. We think that the on-site Si atomic energy differences (thermodynamic

barrier) between the bulk Si (aSi and cSi) and the Li-Si interface region could lead to different Si flux. In particular, the Si flux originates from the bulk Si side in the four models, and the structure and properties of a-Li_xSi regions are proved to be almost identical among the four models in Fig. 3. The only difference is the structural morphologies of Li and Si atoms near the left-side Si/Li-Si interface layers. The corresponding CN_{Li-Si} values at the left-side Si/Li-Si interface position are also different in the four cases in Supplementary Fig. 3. A higher CN_{Li-Si} means more Si atoms around Li atoms in the first coordination shell. We thus speculate that the different atomic structures of the Si/Li-Si interface region, due to the contact of the a-Li_xSi region to the Si materials exposed with different facets, could result in distinct on-site Si atomic energies at the interface. In other words, the Si/Li-Si interface morphology determines the thermodynamic barrier of the Si atoms from the bulk region toward the a-Li_xSi region. We then need to compute the thermodynamic barrier derived from on-site Si atomic energies in the bulk region vs. in the interface region. In addition, the definitions of on-site Si atomic energy and the on-site Si atomic energy difference are introduced in the methods section below.

The on-site Si atomic energy can be defined as the energy change upon removing one Si atom from a specific position in each Si/Li interface models. As displayed in Fig. 4a, we select four distinct regions to obtain various on-site Si atomic energies. The bulk Si atoms are selected from two different Si regions to obtain the $\Delta E_{Si1,b}$ and $\Delta E_{Si2,b}$. We randomly select Si atoms from the Si/Li-Si interface region and a-Li_xSi region to obtain the $\Delta E_{Si/Li-Si,i}$ and ΔE_{a-Li_xSi} . The average on-site Si atomic energies $\overline{\Delta E_{Si1,b}}$, $\overline{\Delta E_{Si2,b}}$, $\overline{\Delta E_{Si/Li-Si,i}}$ and $\overline{\Delta E_{a-Li_xSi}}$ are calculated based on 2000 on-site Si atomic energy data points. The atom-selection ranges for removing Si atoms in those specific regions are listed in Supplementary Table 2.

In Fig. 4b, we show the average on-site Si atomic energies of $\overline{\Delta E_{Si1,b}}$, $\overline{\Delta E_{Si2,b}}$, $\overline{\Delta E_{Si/Li-Si,i}}$ and $\overline{\Delta E_{a-Li_xSi}}$ for the four Si/Li interface models. We can see that the average on-site Si atomic energies $\overline{\Delta E_{a-Li_xSi}}$ in the a-Li_xSi region are similar (~ -7.10 eV) among the four models due to the similarity of structures as discussed above. The $\overline{\Delta E_{Si1,b}}$ values for the three cSi/Li models (~ -8.91 eV) are similar to each other but lower than that of the aSi/Li model (-7.78 eV). This trend is also observed for the $\overline{\Delta E_{Si2,b}}$ values among the four models. The $\overline{\Delta E_{Si/Li-Si,i}}$ values for the Si/Li-Si interface layers with different microstructure morphologies are -6.98 eV, -6.64 eV, -6.80 eV, and -6.51 eV for aSi/Li, cSi(100)/Li, cSi(110)/Li and cSi(111)/Li systems, respectively, indicating that different microscopic structures of the left-side Si/Li-Si interface could lead to distinct on-site Si atomic energies at interfaces.

Then, we calculate the on-site Si atomic energy difference between the Si/Li-Si interface region and the left bulk Si region, denoted as $\Delta\Delta E = \Delta E_{Si/Li-Si,i} - \Delta E_{Si1,b}$, which represents the thermodynamic barrier derived from on-site Si atomic energies in the interface region vs. in the bulk region. We compare the $\Delta\Delta E$ of the four interface models to check if the trend of $\Delta\Delta E$ matches with the order of Si-flux magnitudes in different interface cases. The $\overline{\Delta\Delta E}$ values are 0.80 eV, 2.28 eV, 2.11 eV and 2.39 eV for the aSi/Li, cSi(100)/Li, cSi(110)/Li and cSi(111)/Li models, respectively. It can be clearly seen from Fig. 4b that the trend of on-site Si atomic energy differences exhibits the order of aSi < cSi(110) < cSi(100) < cSi(111). This means that a lower on-site Si atomic energy difference indicates a lower thermodynamic barrier, which could qualitatively lead to a larger Si-flux magnitude. Thus, this qualitative trend of thermodynamic barriers is in good agreement with the trend of Si-flux magnitudes in the four interface models.

In addition, we provide the distribution histograms for $\Delta E_{Si1,b}$, $\Delta E_{Si/Li-Si,i}$, $\Delta\Delta E$ and their corresponding average values in Supplementary Fig. 5 for the four interface models. We can see that the shapes of $\Delta E_{Si1,b}$ distributions are similar among the four Si/Li models. The distribution behavior of $\Delta\Delta E$ simply depends on the $\Delta E_{Si/Li-Si,i}$ in each model. We note that the $\Delta E_{Si/Li-Si,i}$ and $\Delta\Delta E$ distribution histograms of the cSi(110)/Li model exhibit two peaks, which is different to other models that display a single peak. Employing the bootstrapping method, we demonstrate in Supplementary Fig. 6 that the two distinct peaks appear and the overall distribution profiles are similar among the sub-datasets of 1000 $\Delta E_{Si/Li-Si,i}$

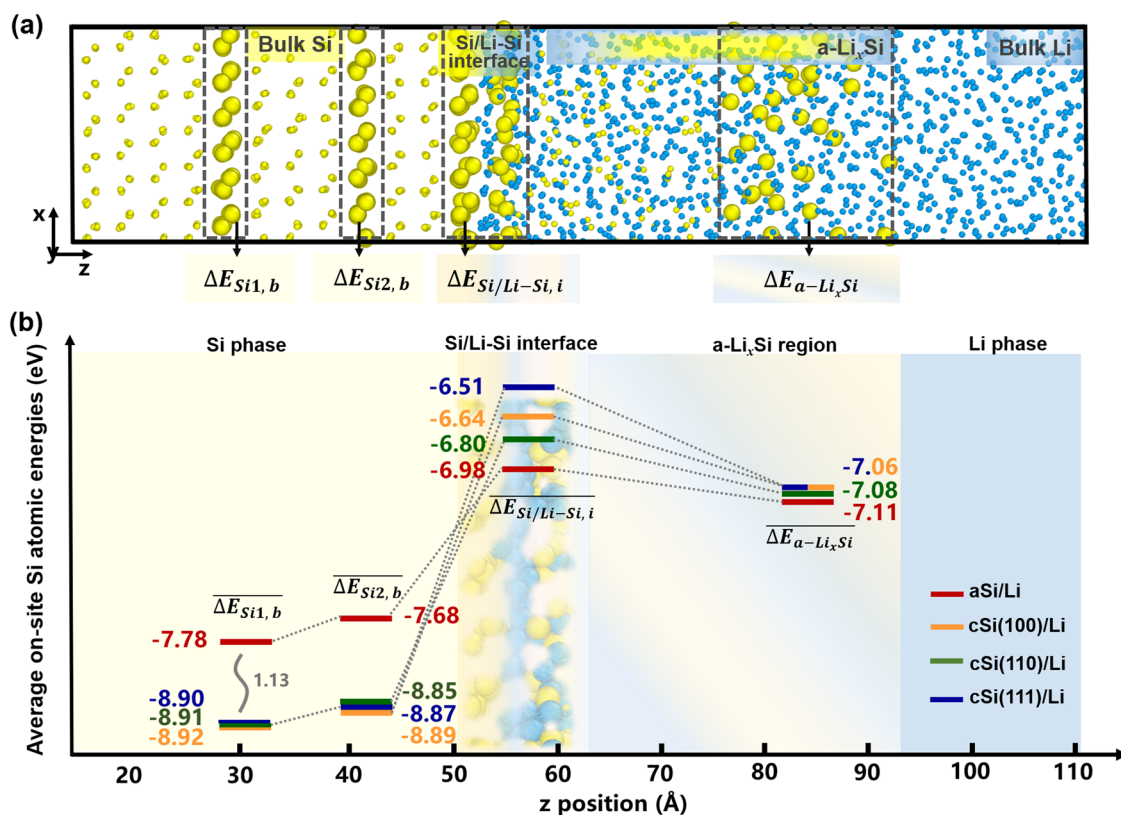


Fig. 4 | Schematic diagram for calculating the on-site Si atomic energy difference. **a** The schematic diagram illustrating the division of distinct regions (with Si atoms represented by large yellow balls) to obtain the on-site Si atomic energies of $\Delta E_{Si1,b}$, $\Delta E_{Si2,b}$, $\Delta E_{Si/Li-Si,i}$ and ΔE_{a-Li_xSi} in the two different bulk Si regions, the Si/Li-Si interface region and the a-Li_xSi region. The four define on-site Si atomic energies represent the energy change upon removal of one Si atom from the left bulk Si region,

the bulk Si region near the Si/Li-Si interface, the Si/Li-Si interface region, and the a-Li_xSi region near the right Li-Si/Li interface, respectively. **b** Diagram of the changes of the average on-site Si atomic energies $\Delta E_{Si1,b}$, $\Delta E_{Si2,b}$, $\Delta E_{Si/Li-Si,i}$ and ΔE_{a-Li_xSi} along the z-axis for the four interface models. Random selection of Si sites for doing statistical averages is introduced in the next methodology section.

points and the complete dataset of 2000 $\Delta E_{Si/Li-Si,i}$ points. Moreover, the atom-selection ranges for removing Si atoms in the four interface models are based on a consistent standard, as shown in Supplementary Table 2. We thus believe that our statistical sampling is sufficient and valid. The above test results also demonstrate the statistical significance of our results regarding the distribution of $\Delta E_{Si/Li-Si,i}$ for the cSi(110)/Li interface case.

Discussion

Therefore, we claim from those results that the Si flux, rather than the Li flux, determines the Li-Si interdiffusion length. We suggest a descriptor that determines the lithiation lengths in the four interface models, which is the on-site Si atomic energy difference between the Si bulk region and the Si/Li-Si interface layers. This enthalpic difference represents a thermodynamic barrier for the Si flux toward the a-Li_xSi region through the Si/Li-Si interface. Since the Si diffusion flux dominates the Li-Si interdiffusion in the interface system as revealed by our MD simulations, a lower on-site Si atomic energy difference between the Si source and the Si/Li-Si interface region could induce a higher Si flux toward the Li side and thereby resulting in a longer Li-Si diffusion extent. In addition, our work suggests that the exposure of Si {110} facets is more favorable in terms of the anode structure design, while the {100} and {111} facets may need to be suppressed in order to promote the Si transforming into the a-Li_xSi phase. This could help reduce inhomogeneous Li/Si distribution and minimize internal stress. Earlier experimental studies¹⁹ also showed that nano-Si grow along [111] direction with the primary {110} planes could enhance the energy density and cycling stability of the Li-Si battery.

In summary, we have revealed kinetic mechanism of Li-Si interdiffusion and microstructural evolution in Li/Si interface models with various Si-facet orientations and phases by using machine learning potential. Our

results are in good agreement with experimental observations, including the Li-Si interdiffusion lengths variation with the order of aSi > cSi(110) > cSi(100) > cSi(111) in our four Li/Si interface models, the evidence of two-phase co-existence during lithiation process, and the high Li concentration accumulated at the Si/Li-Si boundary. More importantly, we demonstrate that the Si flux dominates the heterogeneous Li-Si interdiffusion process, and we further propose a thermodynamic descriptor of the on-site Si atomic energy difference between the Si bulk region and the Si/Li-Si interface layers which directly correlates to the Si flux magnitude. Our results indicate that a larger lithiation length results from a low thermodynamic barrier accompanied by a higher Si flux. Overall, the dynamics of Li-Si interdiffusion and interface morphology evolutions provide important insights into the lithiation mechanism for Si anodes at an atomic-scale level and could guide the optimization design of Si anode materials to enhance homogeneous Li-Si distribution and suppress internal stress.

Methods

Deep potential training and validation

Training. The high-accuracy DP model, which underwent a long training setup using a specific density functional theory (DFT) dataset, was employed to simulate the Li-Si interdiffusion processes. This specific DFT dataset covers the whole compositional space of a/cLi, a/cSi, a/c-Li_xSi (0 < x < 4.5) systems, as labeled in earlier work²⁹. The sizes of embedding and fitting nets were set to three hidden layers, consisting of (25, 50, 100) and (240, 240, 240) neurons, respectively. A cut-off radius 6 Å was used. The starting and final learning rates were set to 1.0×10^{-3} and 1.0×10^{-8} , respectively. A total of 16.0×10^6 steps was set to train the productive DP model. Subsequently, a compressed DP model, derived from the productive DP model, was employed to accelerate and simulate

the Li-Si interdiffusion and structural evolution in the four Li/Si interface models. Detailed exploration and labeling for the DFT dataset can be found in the Li-Si study utilizing the DP method²⁹.

Validation. An independent testing dataset, consisting of a bulk aLi phase (128 atoms), bulk cSi and aSi phases (64 atoms), cSi/Li (96 atoms) and aSi/Li (192 atoms) interface systems, including 500 configurations in total along multiple MD trajectories, to validate the accuracy of our DP model employed for simulating the Li-Si interdiffusion and structural evolution. Those bulk aLi, aSi and cSi configurations were generated at 500 K, the cSi/Li and aSi/Li interface configurations were generated at 300 K (to maintain interfacial morphologies) during DeePMD simulations. Each system ran 20000 steps in the canonical (NVT) ensemble. The initial supercell model of cSi/Li and aSi/Li interface configurations includes a 1 nm vacuum layer, as shown in Supplementary Fig. 1a. The timestep size was set to 0.5 fs. In each system, 100 configurations were selected at equal intervals.

Density functional theory calculations

For the calculations of the DFT dataset, the Projector Augmented Wave (PAW)⁴⁴ potential was used to describe core electrons, and the Perdew–Becke–Ernzerhof (PBE) version of the generalized gradient approximation (GGA) functional was employed to describe the exchange–correlation effect⁴⁵. The kinetic energy cutoff and the mesh grid's k -spacing⁴⁶ were set to 550 eV for the plane-wave basis set and 0.16 \AA^{-1} for the Brillouin zone sampling, respectively. Self-consistent field calculations were converged to 1.0×10^{-6} eV. We used the Vienna ab initio simulation (VASP)⁴⁷ package to generate the DFT dataset.

Deep potential molecular dynamics simulation

As shown in Fig. 1, we constructed four interface models with different Si-facet orientations and phases, namely aSi/Li, cSi(100)/Li, cSi(110)/Li, and cSi(111)/Li to study the dynamics of Li-Si interdiffusion and interfacial structure evolutions. The aSi/Li, cSi(100)/Li and cSi(110)/Li models contain 1536 Si atoms and 3072 Li atoms, and the cSi(111)/Li model contains 1476 Si and 2952 Li atoms. In each model, a 4 nm vacuum layer was introduced on the right side of the Li phase to allow volume variation during Li-Si interdiffusion simulations. Then, we ran DeePMD trajectories under the NVT ensemble for 5 ns at 500 K to analyze the dynamics of Li-Si interdiffusion and morphology distributions. The trajectories were stored every 1 ps and the time step was set to be 0.5 fs. The accurate DP model of Li-Si systems covering the whole compositional space has been demonstrated to be able to well reproduce the thermodynamic properties and phase transformations pathways during Si (de)lithiation process²⁹. We used LAMMPS⁴⁸ package to run all DeePMD simulations.

We note that the strain on the Si lattice cloud influences the Li diffusion into the bulk Si phase. We thus conduct a test for the cSi(110)/Li model to investigate the strain effect. A tensile strain parallel to the Si/Li interface may expand the pore size of bulk Si phase, which could enhance the diffusion of Li atoms into the Si phase. We thus apply a tensile strain on our model to investigate if strain indeed has an impact on the Li diffusion behavior. Here we need to emphasize that the Si lattice constant of the cSi/Li interface model (shown in Fig. 1) in our work is set to be the lattice parameter of a fully relaxed bulk Si. This setup is reasonable because Si is the dominant solid anode material which determines the lattice constants of the Si-Li interface at anode surfaces in batteries. In this test, we apply a 2% tensile strain, which is a quite large strain condition for solid bulk materials. For the cSi(110)/Li interface model, we construct a new supercell box with a 2% tensile strain applied along the x and y directions, and a vacuum region is included along the z direction as well (the supercell parameters along the x , y , and z directions: 22.31 Å, 23.67 Å and 222.69 Å). We then performed DeePMD trajectories under the NVT ensemble condition for 5 ns at 500 K. It can be observed from Supplementary Fig. 7a, b that the Li-Si interdiffusion lengths are 48.5 Å and 47.1 Å for the original and the strained cSi(110)/Li models, respectively, indicating a minor influence on the quantitative values of

interdiffusion lengths. We can also see that the number densities of Li or Si atoms in Supplementary Fig. 7c, d are almost identical between the two models, with further evidences of similar distributions of Li and Si DP-partitioned atomic energies, as depicted in Supplementary Fig. 7e, f. This means that the strain does not apply a significant impact on the Li diffusion toward the Si phase region.

Definitions of key physical quantities

Si flux. The Si flux can be defined as the average number of Si atoms moving from the bulk Si phase toward the Li phase through the Si/Li-Si interface per unit area (nm^2) and per unit time (ns).

Li flux. The Li flux can be defined as the average number of Li atoms moving from the bulk Li phase toward the Si phase through the Si/Li-Si interface per unit area (nm^2) and per unit time (ns).

The DP-partitioned atomic energy $E_{\text{DP-partition}}$. The DP-partitioned atomic energy is obtained directly from the DP model, which partitions the total energy to each atom for a specific configuration. The DP-partitioned atomic energies of Li and Si atoms can be defined as $E(\text{Li})_{\text{DP-partition}}$ and $E(\text{Si})_{\text{DP-partition}}$.

The on-site Si atomic energy ΔE . The energy of a specific Si/Li configuration simulated by DeePMD can be defined as E_{before} . The energy upon removal of one Si atom from this Si/Li configuration can be defined as E_{after} . We then define the on-site Si atomic energy as: $\Delta E = E_{\text{before}} - E_{\text{after}}$, which represents the energy change associated with the removal of a single Si atom from this specific Si/Li configuration. Correspondingly, the on-site Si atomic energies of $\Delta E_{\text{Si1},b}$, $\Delta E_{\text{Si2},b}$, $\Delta E_{\text{Si/Li-Si},i}$ and $\Delta E_{a-\text{Li}_x\text{Si}}$ represent the energy change associated with the removal of one Si atom from the left bulk Si region, the bulk Si region near the Si/Li-Si interface, the Si/Li-Si interface region, and the $a\text{-Li}_x\text{Si}$ region near the right Li-Si/Li interface, respectively. The schematic diagram illustrating the corresponding regions for calculating those on-site Si atomic energies is presented in Fig. 4a. In addition, the atom-selection ranges for removing Si atoms in the four specific regions are listed in Supplementary Table 2. Two parameters are defined to obtain atom-selection ranges: the z -axis position of the Si/Li-Si interface on the left side, denoted as $z_{\text{Si/Li-Si}}$, and the z -axis position of the Li-Si/Li interface on the right side, denoted as $z_{\text{Li-Si/Li}}$. We note that the z -position exhibits different starting and ending points in the three cSi cases with different directions of exposed facets, which can be attributed to distinct distances between two Si layers in these differently oriented models, as presented in Fig. 1.

The average on-site Si atomic energy $\overline{\Delta E}$. To ensure statistical meaning of these on-site Si atomic energies, we chose 40 configurations for each Si/Li system. For each configuration, we randomly removed one Si atom from 50 different Si sites, and obtaining 50 ΔE values. We would have $40 * 50 = 2000$ ΔE values, and then obtain the average on-site Si atomic energy $\overline{\Delta E}$ from these 2000 values. These energy results are the average on-site Si atomic energies presented in the four regions in Fig. 4b, which are defined as $\overline{\Delta E}_{\text{Si1},b}$, $\overline{\Delta E}_{\text{Si2},b}$, $\overline{\Delta E}_{\text{Si/Li-Si},i}$ and $\overline{\Delta E}_{a-\text{Li}_x\text{Si}}$, respectively.

The on-site Si atomic energy difference $\Delta \Delta E$. We further define the on-site Si atomic energy difference between the Li-Si interface and the left bulk Si regions as $\Delta \Delta E = \overline{\Delta E}_{\text{Si/Li-Si},i} - \overline{\Delta E}_{\text{Si1},b}$, which represents the thermodynamic barrier derived from on-site Si atomic energies in the bulk region vs. in the interface region. The average on-site Si atomic energy difference $\overline{\Delta \Delta E}$ can be obtained from these 2000 $\Delta \Delta E$ values or $\overline{\Delta \Delta E} = \overline{\Delta E}_{\text{Si/Li-Si},i} - \overline{\Delta E}_{\text{Si1},b}$.

Additional information

The supplementary information file provides the supercell parameters, the atom-selection ranges for removing Si atoms in the left bulk Si phase, the

bulk Si region near the Si/Li-Si interface, the Si/Li-Si interface region and the a-Li₂Si region near the right Li-Si/Li interface for the four Si/Li interface models. We present the results of energies and forces predicted by the DP model and those calculated by DFT method, the distribution of maximum deviation of forces, the average Li-Si coordination numbers (CN_{Li-Si}), and the average DP-partitioned atomic energy distributions of Li and Si atoms for the four Si/Li interface models. Distributions of the on-site Si atomic energies $\Delta E_{Si,b}$ and $\Delta E_{Si/Li-Si,i}$, as well as the on-site Si atomic energy difference $\Delta \Delta E$ between $\Delta E_{Si,b}$ and $\Delta E_{Si/Li-Si,i}$, are shown for the four Si/Li interface models. We compare various distributions of the on-site Si atomic energies $\Delta E_{Si/Li-Si,i}$ to validate the statistical significance using the bootstrapping method for the cSi(100)/Li interface model. The average Li concentration profiles, number density and DP-partitioned atomic energy distributions of Li and Si atoms are compared between the cSi(110)/Li interface model without strain and the model with a 2% tensile strain.

Data availability

The productive and compressed DP models, and the DFT dataset are open source and can be obtained through the following link: <https://www.aissquare.com/datasets/detail?pageType=datasets&name=LiSi-PBE-DFT-dataset&id=85>.

Received: 9 February 2024; Accepted: 14 June 2024;

Published online: 25 June 2024

References

- Tang, Y., Zhang, Y., Li, W., Ma, B. & Chen, X. Rational material design for ultrafast rechargeable lithium-ion batteries. *Chem. Soc. Rev.* **44**, 5926–5940 (2015).
- Schmich, R., Wagner, R., Höppl, G., Placke, T. & Winter, M. Performance and cost of materials for lithium-based rechargeable automotive batteries. *Nat. Energy* **3**, 267–278 (2018).
- McDowell, M. T., Lee, S. W., Nix, W. D. & Cui, Y. 25th anniversary article: Understanding the lithiation of silicon and other alloying anodes for lithium-ion batteries. *Adv. Mater.* **25**, 4966–4985 (2013).
- Obrovac, M. N. & Chevrier, V. L. Alloy negative electrodes for Li-ion batteries. *Chem. Rev.* **114**, 11444–11502 (2014).
- Xu, Z. L., Liu, X., Luo, Y., Zhou, L. & Kim, J. K. Nanosilicon anodes for high performance rechargeable batteries. *Prog. Mater. Sci.* **90**, 1–44 (2017).
- Feng, K. et al. Silicon-based anodes for lithium-ion batteries: from fundamentals to practical applications. *Small* **14**, 1702737 (2018).
- Balke, N. et al. Real space mapping of Li-ion transport in amorphous Si anodes with nanometer resolution. *Nano Lett.* **10**, 3420–3425 (2010).
- Rehnlund, D., Wang, Z. & Nyholm, L. Lithium-diffusion induced capacity losses in lithium-based batteries. *Adv. Mater.* **34**, 2108827 (2022).
- Key, B., Morcrette, M., Tarascon, J. M. & Grey, C. P. Pair distribution function analysis and solid state NMR studies of silicon electrodes for lithium ion batteries: Understanding the (de)lithiation mechanisms. *J. Am. Chem. Soc.* **133**, 503–512 (2011).
- Liu, X. H. et al. In situ atomic-scale imaging of electrochemical lithiation in silicon. *Nat. Nanotechnol.* **7**, 749–756 (2012).
- Wang, J. W. et al. Two-phase electrochemical lithiation in amorphous silicon. *Nano Lett.* **13**, 709–715 (2013).
- Ogata, K. et al. Revealing lithium-silicide phase transformations in nano-structured silicon-based lithium ion batteries via in situ NMR spectroscopy. *Nat. Commun.* **5**, 3217 (2014).
- McDowell, M. T. et al. In situ TEM of two-phase lithiation of amorphous silicon nanospheres. *Nano Lett.* **13**, 758–764 (2013).
- Lee, S. W., McDowell, M. T., Choi, J. W. & Cui, Y. Anomalous shape changes of silicon nanopillars by electrochemical lithiation. *Nano Lett.* **11**, 3034–3039 (2011).
- Lee, S. W., McDowell, M. T., Berla, L. A., Nix, W. D. & Cui, Y. Fracture of crystalline silicon nanopillars during electrochemical lithium insertion. *Proc. Natl Acad. Sci. USA* **109**, 4080–4085 (2012).
- McDowell, M. T. et al. Studying the kinetics of crystalline silicon nanoparticle lithiation with in situ transmission electron microscopy. *Adv. Mater.* **24**, 6034–6041 (2012).
- Liu, X. H. et al. Anisotropic swelling and fracture of silicon nanowires during lithiation. *Nano Lett.* **11**, 3312–3318 (2011).
- Zhao, X. & Lehto, V. P. Challenges and prospects of nanosized silicon anodes in lithium-ion batteries. *Nanotechnology* **32**, 042002 (2021).
- Zhang, Z. et al. Confining invasion directions of Li⁺ to achieve efficient Si anode material for lithium-ion batteries. *Energy Storage Mater.* **42**, 231–239 (2021).
- Chan, M. K. Y., Wolverton, C. & Greeley, J. P. First principles simulations of the electrochemical lithiation and delithiation of faceted crystalline silicon. *J. Am. Chem. Soc.* **134**, 14362–14374 (2012).
- Kim, S. P., Datta, D. & Shenoy, V. B. Atomistic mechanisms of phase boundary evolution during initial lithiation of crystalline silicon. *J. Phys. Chem. C* **118**, 17247–17253 (2014).
- Ostadosse, A. et al. Stress effects on the initial lithiation of crystalline silicon nanowires: reactive molecular dynamics simulations using ReaxFF. *Phys. Chem. Chem. Phys.* **17**, 3832–3840 (2015).
- Fernandez, F., Paz, S. A., Otero, M., Barraco, D. & Leiva, E. P. M. Characterization of amorphous Li_xSi structures from ReaxFF via accelerated exploration of local minima. *Phys. Chem. Chem. Phys.* **23**, 16776–16784 (2021).
- Kirsch, C., Drebl, C. & Sebastiani, D. Atomistic diffusion pathways of lithium ions in crystalline lithium silicides from ab initio molecular dynamics simulations. *J. Phys. Chem. C* **126**, 12136–12149 (2022).
- Kim, K. J. & Qi, Y. Vacancies in Si can improve the concentration-dependent lithiation rate: Molecular dynamics studies of lithiation dynamics of Si electrodes. *J. Phys. Chem. C* **119**, 24265–24275 (2015).
- Deringer, V. L. Modelling and understanding battery materials with machine-learning-driven atomistic simulations. *J. Phys. Energy* **2**, 041003 (2020).
- De Vasconcelos, L. S. et al. Chemomechanics of rechargeable batteries: Status, theories, and perspectives. *Chem. Rev.* **122**, 13043–13107 (2022).
- Artrith, N., Urban, A. & Ceder, G. Constructing first-principles phase diagrams of amorphous Li_xSi using machine-learning-assisted sampling with an evolutionary algorithm. *J. Chem. Phys.* **148**, 241711 (2018).
- Fu, F. et al. Unraveling the atomic-scale mechanism of phase transformations and structural evolutions during (de)lithiation in Si anodes. *Adv. Funct. Mater.* **33**, 2303936 (2023).
- Tuo, P. et al. Spontaneous hybrid nano-domain behavior of the organic-inorganic hybrid perovskites. *Adv. Funct. Mater.* **33**, 2301663 (2023).
- Hu, T. et al. Impact of the local environment on Li ion transport in inorganic components of solid electrolyte interphases. *J. Am. Chem. Soc.* **145**, 1327–1333 (2023).
- Hu, T., Dai, F. Z., Zhou, G., Wang, X. & Xu, S. Unraveling the dynamic correlations between transition metal migration and the oxygen dimer formation in the highly delithiated Li_xCoO₂ Cathode. *J. Phys. Chem. Lett.* **14**, 3677–3684 (2023).
- Bekaert, L. et al. Assessing the reactivity of the Na₃PS₄ solid-state electrolyte with the sodium metal negative electrode using total trajectory analysis with neural-network potential molecular dynamics. *J. Phys. Chem. C* **127**, 8503–8514 (2023).
- Bekaert, L. et al. Increasing the sodium metal electrode compatibility with the Na₃PS₄ solid-state electrolyte through heteroatom substitution. *ChemSusChem* **16**, e202300676 (2023).
- Zhang, L., Han, J., Wang, H., Car, R. & Weinan, E. Deep potential molecular dynamics: A scalable model with the accuracy of quantum mechanics. *Phys. Rev. Lett.* **120**, 143001 (2018).
- Zhang, Y. et al. DP-GEN: A concurrent learning platform for the generation of reliable deep learning based potential energy models. *Comput. Phys. Commun.* **253**, 107206 (2020).

37. Wang, H. et al. Atomistic modeling of lithium materials from deep learning potential with ab initio accuracy. *Chin. J. Chem. Phys.* **36**, 573–581 (2023).
38. Li, W. & Ando, Y. Effect of local structural disorder on lithium diffusion behavior in amorphous silicon. *Phys. Rev. Mater.* **4**, 45602 (2020).
39. Onat, B., Cubuk, E. D., Malone, B. D. & Kaxiras, E. Implanted neural network potentials: Application to Li-Si alloys. *Phys. Rev. B* **97**, 094106 (2018).
40. Wen, T., Zhang, L., Wang, H., Weinan, E. & Srolovitz, D. J. Deep potentials for materials science. *Mater. Future* **1**, 022601 (2022).
41. Liu, X. H. et al. Size-dependent fracture of silicon nanoparticles during lithiation. *ACS Nano* **6**, 1522–1531 (2012).
42. Yang, H. et al. A chemo-mechanical model of lithiation in silicon. *J. Mech. Phys. Solids* **70**, 349–361 (2014).
43. Gu, M. et al. Electronic origin for the phase transition from amorphous Li_xSi to crystalline $\text{Li}_{15}\text{Si}_4$. *ACS Nano* **7**, 6303–6309 (2013).
44. Joubert, D. From ultrasoft pseudopotentials to the projector augmented-wave method. *Phys. Rev. B* **59**, 1758–1775 (1999).
45. Perdew, J. P., Burke, K. & Ernzerhof, M. Generalized gradient approximation made simple. *Phys. Rev. Lett.* **78**, 1396–1396 (1997).
46. Monkhorst, H. J. & Pack, J. D. Special points for brillonin-zone integrations. *Phys. Rev. B* **13**, 5188–5192 (1976).
47. Kresse, G. & Furthmüller, J. Efficiency of ab-initio total energy calculations for metals and semiconductors using a plane-wave basis set. *Comput. Mater. Sci.* **6**, 15–50 (1996).
48. Plimpton, S. Fast parallel algorithms for short-range molecular dynamics. *J. Comput. Phys.* **117**, 1–19 (1995).

Acknowledgements

The authors gratefully acknowledge funding support from the Ministry of Science and Technology of People's Republic of China (Grant No. 2021YFB3800303), DP Technology Corporation (Grant No. 2021110016001141), the National Natural Science Foundation of China (Grants No. 22008096). The computing resource of this work was provided by the Bohrium Cloud Platform (<https://bohrium.dp.tech>), which is supported by DP Technology.

Author contributions

F.F., S.X., and F.Z.D. conceived and designed this project. F.F. performed simulations and wrote the original manuscript. S.X. and F.Z.D. revised the manuscript. X.W., T.H., and G.Z. supported discussion and data analysis. All the authors participated in the reviewing and editing of the manuscript.

Competing interests

The authors declare no competing interests.

Additional information

Supplementary information The online version contains supplementary material available at <https://doi.org/10.1038/s41524-024-01327-1>.

Correspondence and requests for materials should be addressed to Fu-Zhi Dai or Shenzhen Xu.

Reprints and permissions information is available at <http://www.nature.com/reprints>

Publisher's note Springer Nature remains neutral with regard to jurisdictional claims in published maps and institutional affiliations.

Open Access This article is licensed under a Creative Commons Attribution 4.0 International License, which permits use, sharing, adaptation, distribution and reproduction in any medium or format, as long as you give appropriate credit to the original author(s) and the source, provide a link to the Creative Commons licence, and indicate if changes were made. The images or other third party material in this article are included in the article's Creative Commons licence, unless indicated otherwise in a credit line to the material. If material is not included in the article's Creative Commons licence and your intended use is not permitted by statutory regulation or exceeds the permitted use, you will need to obtain permission directly from the copyright holder. To view a copy of this licence, visit <http://creativecommons.org/licenses/by/4.0/>.

© The Author(s) 2024